Light-emitting transistors based on solution processed heterostructures of self-organized multiple quantum well perovskite and metal-oxide semiconductors

Mujeeb Ullah Chaudhry,[*1] *Nana Wang,*[2] *Kornelius Tetzner,*[3] *Akmaral Seitkhan,*[4] *Yanfeng Miao,*[2] *Yan Sun,*[2] *Michael C. Petty,*[1] *Thomas D. Anthopoulos,*[*3, 4] *Jianpu Wang,*[*2] *Donal D.C. Bradley*[*5]

[1] Department of Engineering, Durham University, Lower Mount Joy, South Road, Durham, DH1 3LE, United Kingdom.

[2] Key Laboratory of Flexible Electronics (KLOFE) & Institute of Advanced Materials (IAM), Jiangsu National Synergetic Innovation Center for Advanced Materials (SICAM), Nanjing Tech University (NanjingTech), 30 South Puzhu Road, Nanjing 211816, P.R. China.

[3]Department of Physics and Centre for Plastic Electronics, Blackett Laboratory, Imperial College London, London SW7 2BW, United Kingdom.

[4] King Abdullah University of Science and Technology (KAUST), KAUST Solar Center, Physical Science and Engineering Division, Thuwal 23955, Saudi Arabia.

[5] Departments of Physics and Engineering Science, Division of Mathematical, Physical and Life Sciences, University of Oxford, 9 Parks Road, Oxford OX1 3PD, United Kingdom.

*Address correspondence to: mujeeb.u.chaudhry@durham.ac.uk; iamjpwang@njtech.edu.cn; thomas.anthopoulos@imperial.ac.uk; donal.bradley@mpls.ox.ac.uk

Abstract

Solution-processed hybrid organic-inorganic perovskite semiconductors have demonstrated remarkable performance for both photovoltaic and light-emitting-diode applications in recent years, launching a new field of condensed matter physics. However, their use in additional emerging opto-electronic applications such as light-emitting field effect (LEFET) transistors has been surprisingly limited with only a few exceptions with low performance. We report the development of hybrid light-emitting field-effect transistors (LEFETs) consisting of a solution processed self-organized multiple quantum well (MQW) lead iodide perovskite layer grown onto an electron transporting In_2O_3/ZnO heterojunction channel. The multi-layer transistors offer bi-functional characteristics, namely transistor function with high electron mobility (>20 cm^2/Vs) and a large current On/Off ratio (>10^6), combined with near infrared (NIR) light emission (λ_{max} = 783 nm) with a promising external quantum efficiency (≈ 0.2 % at 18 cd/m^2). A further interesting feature of these hybrid LEFETs, in comparison to previously reported structures, is their highly uniform and stable emission characteristics, which make them attractive for smart-pixel-format display applications.

Organometal halide perovskite semiconductors possess highly attractive optoelectronic properties,[1-10] which combined with cost-effective solution processing have fuelled growing interest in photovoltaic,[5-13] water splitting,[14] light-emitting diode (LED),[15-18] optically-pumped laser,[19-21] and X-ray detector[22, 23] applications. The combination of high photoluminescence quantum efficiency[2] (PLQE), high ambipolar charge carrier mobility[24-26] and widely tuneable optical gaps (spanning the visible to near infrared spectrum)[26] is of especial interest for LEDs,[15-18] light-emitting field effect transistors (LEFETs)[27-29] and lasers.[30,31] LEFETs, in particular, integrate the switching functionality of FETs with the light emission properties of an LED.[32] Although LEFETs demand simultaneous optimisation of multiple electrical and optical device characteristics,[32-34] they are highly attractive for applications in optical communications and high-definition displays due to their potential for simplifying and maximising the emissive aperture ratio of the pixel.[32-38]

In the case of perovskite LEFETs (PeLEFETs), there has been rather little progress since the first report in 2015 of methylammonium lead iodide ($CH_3NH_3PbI_3$) devices.[27] Light emission was observed only at temperatures ≤ 178 K, with charge carrier mobilities limited to $\approx 10^{-5}$ cm^2/Vs. Subsequent AC driving at high frequency allows room temperature emission by suppressing ion migration but with low (unquantified) intensity.[28] At low temperature the emission is stronger and quantifiable, but only reaches a luminance of 0.94 cd/m^2 at 78K for 100kHz driving.[29] This is despite the remarkable progress achieved in the area of perovskite-based LEDs (EQEs >14%)[39] and the predictions for ultra-high electron ($\mu_e \approx 1{,}500$ cm^2/Vs) and hole ($\mu_h \approx 3{,}100$ cm^2/Vs) mobility.[24,25,26] This limited progress is likely due to the microstructure of the three-dimensional (3D) perovskite layers[15-16] which have often been employed, and the adverse effects of ion migration and polarization disorder.[40]

More recently, a new class of self-organized multiple quantum well (MQW) perovskite has been demonstrated.[18,36] This class of perovskite combines high photoluminescence quantum efficiency, PLQE ($\Phi \approx 60$ %) with superior layer uniformity manifested as low surface roughness (rms ≈ 2.6 nm). Red/near-infrared (λ_{max} = 791 nm) and green (λ_{max} = 532 nm) MQWs perovskite LEDs have been reported, with state-of-the-art external quantum efficiency (EQE) values of 12.7% and 15.5%, respectively.[41-44] Sky-blue LED devices have also been reported with EQE up to 1.5%.[45] In comparison to lead halide perovskites, solution-processed metal-oxide semiconductors are known to yield high performance transistors and integrated circuits,[46-48] with electron mobilities reaching ≈ 50 cm^2/Vs for structures based on oxide-oxide heterojunctions which promote the formation of a two-dimensional-like electron gas.[47] These latter materials do not, however, give efficient light emission and so are not suited on their own to LEFET use.

Herein we report the development of an innovative strategy that combines these two classes of material in a heterostructure PeLEFET architecture. This heterostructure consists of a self-organized $NFPI_7$ (*vide infra*) MQW perovskite as the light-emitting and hole-transporting layer, together with a high electron mobility In_2O_3/ZnO heterostructure in a layered channel configuration. The combination yields relatively efficient (0.2% EQE at 18 cd/m^2) PeLEFETs operating at room temperature, with effective electron mobilities of the order of ~ 20 cm^2/Vs and a high channel current On/Off ratio $>10^6$. Light emission emerges uniformly from the entire drain electrode region (hole injecting contact) and peaks in the near infra-red at 783 nm (a wavelength widely used for fluorescence-free Raman spectroscopy)[49], with a full-width-at-half-maximum linewidth $\Delta\lambda$ = 50 nm that ensures enough visible red light for it to be readily observable by eye. The electrical and optical performance of the PeLEFETs studied here is orders of magnitude better than previously reported and offers encouragement for further progress towards a variety of solution processed inorganic optoelectronic devices.

A schematic of the perovskite MQW structure, referred to hereafter as $NFPI_7$, is shown in **Fig. 1(a)**. $NFPI_7$ films were deposited by spin-coating a precursor solution comprising 1-naphthylmethylamine iodide (NMAI), formamidinium iodide (FAI) and PbI_2 in molar ratio 2:1:2 dissolved in N,N-dimethylformamide (DMF) (7 wt.%) and annealed at 100 ^oC for 10 min (see Experimental Methods for details). Atomic force microscopy (AFM) measurements on typical 20 nm thickness $NFPI_7$ films show uniform surface coverage with 2 nm root-mean-square roughness (see **Fig. 1(b**)). To investigate further the film structure, X-ray diffraction (XRD) measurements (see **Fig. 1(c**)) were performed on $NFPI_7$ films deposited on ZnO/PEIE coated spectrosil substrates. These show clear evidence for layered perovskite structures with XRD peaks at 7.3, 11.0, 13.9, 25.7, 28.1 and 29.3°.[50,51] Thin film absorption spectra (see **Fig. 2(a)**) for $NFPI_7$ deposited on ZnO/PEIE coated spectrosil substrates also exhibit exciton spectral features characteristic of MQW perovskite materials[18,52] with a strong absorption peak at 567 nm and shoulders at 632 and 760 nm, indicative of at least four different QW bandgaps with single, double, triple and quadruple PbI_6^{4-} layers. The corresponding photoluminescence (PL) spectrum shows a dominant emission peak at 783 nm with much weaker peaks at 572, 640 and 678 nm, indicative of efficient energy transfer between the different QWs.[18] A high PLQE results, with $\Phi_{max} \approx 66\%$ at excitation intensity $I_{ex} \approx 0.3$ mW cm^{-2} (see **Fig. 2(b)**). A consistently long PL decay time of ~ 20 ns at 4 nJ cm^{-2} per pulse excitation (see **Fig. 2(c)**) is also observed.

Fig. 3(a) shows a schematic structure for the $NFPI_7$-based PeLEFETs. Devices were fabricated on commercially sourced Si^{++}/SiN_x substrates with a 400 nm-thick SiN_x layer onto which In_2O_3/ZnO heterojunction layers were sequentially deposited by spin-coating from solution (details of the process are provided in the **Experimental Method** section below). A 30 nm thickness, shadow mask delineated (0.225 × 10 mm^2), electron-injecting Al source electrode was next deposited directly on top of the In_2O_3/ZnO heterojunction by thermal

evaporation *in vacuo* (≈10^{-6} mbar). An ultrathin layer of ethoxylated polyethylenimine (PEIE) was then coated from 2-methoxyethanol solution across the entire substrate before the 20 nm thickness $NFPI_7$ perovskite MQW film was deposited on top. Finally, the MoO_x/Au (5/20 nm) hole-injecting drain electrode (0.25 × 10 mm^2) was evaporated using a complementary shadow-mask to complete the non-planar source-drain geometry, with a 100 μm channel length and 14 mm width. Further details of the fabrication are provided below (**Experimental Method**), together with device testing protocols.

The energy levels for the two electrodes, MoO_x and PEIE interlayer materials, and the $NFPI_7$ MQW semiconductor are shown in **Fig. 3(b)**. The energy level values for PEIE-modified ZnO were measured using a scanning Kelvin Probe system and for $NFPI_7$ films were estimated using ultraviolet photoelectron spectroscopy and optical measurements as reported previously.[18] The operating mechanism of the $NFPI_7$-based PeLEFETs can be visualized from the energy levels shown in **Fig. 3(b)** and the schematics of charge transport and injection given in Supporting Information **Fig. S5**. Electrons are injected from the Al (- 4.1 eV work function) source electrode into the In_2O_3/ZnO layer (- 4.2 eV Fermi level) and travel in-plane across the channel at the SiN_x dielectric and metal-oxide semiconductor interface (through the accumulation region). The channel electrons are then injected into the $NFPI_7$ film under V_{DS} bias, with the PEIE interlayer supporting efficient electron injection from the metal-oxide semiconductor bilayer; PEIE is a well-known electron injection interlayer for use with perovskite[16] and other semiconductors.[34,54] Holes are injected into the $NFPI_7$ film directly from the MoO_x/Au drain electrode (-5.4 eV work function) and combine with the injected electrons to form excitons, which decay radiatively to give light emission.

Cross-sectional TEM images (see **Figure 3(c)**) of device structures without the top MoO_x/Au drain electrode and in a region away from the Al source electrode reveal the expected layers with distinct boundaries. In_2O_3 forms a particularly smooth and homogenous layer on

top of the Si^{++}/SiN_x substrate, while ZnO demonstrates higher roughness (rms = ~ 1.2 nm). The imaged thicknesses of the In_2O_3, ZnO, and $NFPI_7$ layers are 6-7, 8-10, and 18-20 nm, respectively. Energy dispersive X-ray spectroscopy (EDS) mapping for specific atoms confirmed the homogeneity and low intermixing of the layers. In, Zn and Pb maps align, as expected, exclusively with the In_2O_3, ZnO and $NFPI_7$ layers, respectively. Oxygen maps show the expected high concentration in the oxide layers, with a low content in the $NFPI_7$ layer but high concentration again in the top C/Pt protective layer (Supporting Information **Fig. S1**). The drain electrode is semi-transparent (see Supporting Information **Fig. S2**) so light generated within the perovskite layer can be coupled out of the LEFET.

Figure 4(a) shows the room temperature saturation regime electrical transfer characteristics for a PeLEFET together with a plot of the square root of the drain current versus gate voltage. The PeLEFET shows clear n-channel transistor behaviour with modest hysteresis and on/off current ratio $>10^6$. The linear fit (red line) to the square root of the drain current is used to calculate the electron mobility (μ_e) which is ≈ 28 cm^2/Vs. However, the square root of the drain current shows a non-ideal curve and hence, field-effect electron mobility was recalculated following a recently suggested methodology[55] to correct for the non-ideal characteristics (reliability factor = 77 %). We estimate an effective mobility $\mu_e \approx 20$ $cm^2\ V^{-1}\ s^{-1}$ (Supporting Information **Fig. S3** and **Table S1**).

The good PeLEFET device performance is then expected to arise from electrons being efficiently injected from the In_2O_3/ZnO heterojunction channel into the $NFPI_7$ layer after drifting along the SiN_X-In_2O_3/ZnO interface. They will combine there with holes injected from the drain electrode, with a working hypothesis that whilst holes are readily injected from the MoO_x/Au drain electrode into the $NFPI_7$ layer, their low mobility[18] prevents formation of a measurable hole accumulation layer. In this respect the device has the semblance of a LED structure that shares its two electrodes with an entangled unipolar FET structure.

The electrical and optical (electroluminescence, EL) output characteristics of the PeLEFET are shown in **Figure 4(b)**. The optical output characteristics show a high turn-on voltage (~17 V), while the electrical output curves reveal a sigmoidal behaviour at lower V_{DS}, which is indicative of the presence of significant contact resistance (R_C).[53] This is somewhat surprising since the In_2O_3/ZnO heterojunction channel [47,53] is known to exhibit small R_C and, as such, linear I_D *vs* V_D curves at low source-drain fields. We thus hypothesize that the apparent R_C for electrons originates mainly from the residual injection barrier at the interface between ZnO/PEIE and the light-emitting $NFPI_7$ layer (**Fig. 3(b)**). **Table-1** summarises the electrical and optical characteristics of the PeLEFETs together with literature values for comparison. Evidently, the PeLEFET performance achieved here represents the current state-of-the-art.

Fig. 5(a) shows the current density and EL power (note inverted scale for ease of viewing) as a function of gate voltage in the saturation regime (V_{DS} = 50 V). The current density (J) was calculated as the channel current passing through the light emitting drain electrode divided by its area. A maximum luminance of 18 cd/m^2 was calculated at gate bias of 50 V. **Fig. 5(b)** displays the luminance and external quantum efficiency [EQE (%)] versus J_{DS} at different V_G potentials (Supporting Information **Fig. S4**). An EQE value of 0.2% was calculated at drain current density J_{DS} = 2.5 A/cm^2, whilst the maximum radiative recombination efficiency (internal quantum efficiency, IQE) was 6 % at 18 cd/m^2 luminance (see Supporting Information **Table S2**). The modest (in absolute terms) IQE, despite the high PLQE of the $NFPI_7$ layer (60%), suggests that there is an imbalance in carrier injection/transport. Given the n-channel behaviour observed in **Fig. 4(a),** it would appear that an excess of electrons accumulates in the channel and is eventually injected into the $NFPI_7$. An improved charge balance, or confinement, would help to boost the EL efficiency and will be a focus for future studies.

Optical micrographs recorded during device operation are shown in **Fig. 5(c)**. As can be seen the devices show uniform red emission emerging from under the MoO_x/Au drain electrode. The EL emission spectrum (**Fig. 5(d)**) peaks in the NIR at 783 nm and only appears red as a result of the filtering effect of the digital camera response. The observed emission area encouragingly suggests that hole injection occurs rather uniformly across the whole of the drain electrode region. The resulting large emission area is spatially stable and independent of V_G (between 0-50 V). This is an important observation and is consistent with the behaviour recently observed for certain polymer LEFETs.[33,34] It eliminates the small area, V_{GS}-dependent/electrode-edge-confined, uneven stripe emission that has often been seen for LEFETs.[27-32]

The results presented here represent a significant advance over previously reported PeLEFETs and can be seen as an important step towards a new class of perovskite optoelectronic devices. The use of PEIE[54] in these PeLEFETs has a positive effect in three ways: (i) It lowers the surface potential of ZnO to improve the deposition of $NFPI_7$ on top,[18] (ii) it lowers the electron injection barrier between ZnO and $NFPI_7$, and (iii) it helps to ensure that the EL emission emerges uniformly from under the drain MoO_x/Au electrode.[33,34] A higher efficiency can, therefore, be expected for a more transparent drain electrode and again this will be a focus for future study.

In summary, we report the development of efficient red/NIR light-emitting transistors based on the solution processed self-organized multiple quantum well perovskite $NFPI_7$ and an n-channel In_2O_3/ZnO heterojunction semiconductor, acting as the hole-transporting/light-emitting and electron transporting layers, respectively. The In_2O_3/ZnO heterojunction was shown to act as a gate-tunable electron injecting contact for the light-emitting $NFPI_7$ layer, which in turn enabled bifunctional device operation (i.e. electrical switching and light-emission) at room temperature. Important characteristics of the hybrid In_2O_3/ZnO/$NFPI_7$ light-

emitting transistors include, large-area and uniform NIR-peaked light-emission, and an appreciable EQE value of 0.2% at a current density of 2.5 A/cm^2. Our results demonstrate the viability of using $NFPI_7$ and related 2D perovskites in combination with super-lattice metal-oxide semiconductors for high-performance PeLEFETs, a promising partnership for next generation optoelectronic devices.

Experimental Method

Device Fabrication: The PeLEFETs (see **Fig. 3(a)** schematic) used in this study were fabricated on Si/SiN_x wafers (Active Business Company GmbH) with the 400 nm SiN_x dielectric layer grown by low pressure chemical vapor deposition (LPCVD). The wafers were diced into smaller device substrates (15 × 15 mm^2), each containing a uniform Si^{++} doped gate electrode beneath the SiN_x dielectric layer. They were cleaned by ultra-sonication in acetone for 15 min, followed by 15 min in 2-propanol and dried using pressurized nitrogen.

Separate In_2O_3 and ZnO precursor solutions were prepared by dissolving, under constant stirring at room temperature, respectively 20 mg/mL indium nitrate hydrate ($In(NO_3)_3{\cdot}xH_2O$, 99.99%, Indium Corporation) in 2-methoxyethanol (99.8%, Sigma-Aldrich) and 10 mg/mL zinc oxide (ZnO, 99.99%, Sigma-Aldrich) nanoparticles in aqueous ammonium hydroxide solution (NH_4OH, 50% v/v aqueous solution, Alfar Aesar). The In_2O_3 and ZnO precursor solutions were sequentially deposited by spin-coating at 4000 rpm for 30 s onto the Si/SiN_x substrates, with thermal annealing on a hotplate at 300 °C for 1 hour after each deposition to form the required In_2O_3 and ZnO layers.

The PEIE films were prepared by spin-coating a solution of PEIE in 2-methoxyethanol (0.4 wt%) onto the ZnO layer with source electrode (see below) at 5,000 rpm, followed by

rinsing twice with DMF to leave an ultrathin layer.[16, 54] The perovskite precursor was prepared by dissolving NMAI, FAI and PbI_2 at a molar ratio of 2:1:2 in DMF.[18] This solution was then spin-coated onto the PEIE-treated ZnO at 3,000 rpm and annealed at 100 ^oC for 10 min to form the $NFPI_7$ layer.

Complementary multiple-finger shadow masks were used, in sequence, to deposit separately the interdigitated source and drain electrodes, using thermal evaporation. The electron injecting Al source electrode was positioned directly on top of the ZnO layer using the first mask. Next the ultrathin (~1 nm) PEIE and 20 nm $NFPI_7$ perovskite layers were formed (see above). Finally, the MoO_x/Au (5/20 nm) hole injecting drain electrode was deposited on top of the $NFPI_7$ using the second shadow mask, resulting in an asymmetric, interdigitated finger array as shown in **Fig. 3(a)** and Supporting Information **Fig. S5**. The resulting PeLEFET channel width and length were measured (using a scaled optical microscope image) to be 14 mm and 100 μm, respectively.

Optical, Electrical and Structural Characterization: Absorption spectra for thin film samples were measured using a Cary 5000 (Agilent) ultraviolet–visible spectrophotometer, equipped with an integrating sphere. PL spectra and transient PL decays were measured using an Edinburgh Instruments FLS 980 spectrofluorometer equipped with a 445 nm pulsed laser. PLQE measurements used an integrating-sphere-based system equipped with 445 nm CW laser excitation, optical fiber collection and a QE65 Pro spectrometer from Ocean Optics.[56]

The electrical characteristics of the devices were tested within a nitrogen-filled glove box using an Agilent B2902A semiconductor parameter analyzer and probe-station. For electroluminescence characterization, a calibrated photodiode (Konica Minolta LS-100 luminance meter) was attached to the probe-station so that it was positioned vertically above the active region of the device. Microscopic images of PeLEFETs in operation were taken

using a digital camera that replaced the LS-100 luminance meter. EL power and EQE values were calculated for the PeLEFETs under the assumption of Lambertian emission as observed previously for $NFPI_7$ LEDs.[18,32-34,38] EL spectra were recorded using an Ocean-Optics USB2000+ spectrometer equipped with optical fiber collection optics that were attached to the probe-station in place of the camera.

The PeLEFET charge carrier mobility was calculated from the electrical transfer characteristics in the saturation regime, using the equation:

$$I_{DS} = \frac{W\, C_i\, \mu}{2 \times L}(V_{GS} - V_{TH})^2$$

where I_{DS} is the experimentally measured drain-source current, W/L is the geometric width-to-length ratio for the device channel, V_{GS} is the gate-source voltage and C_i is the geometrical capacitance of the dielectric. The calculated mobility was corrected for the non-ideality of the device characteristics (using the Choi *et al*[55] reliability factor) thereby yielding a more reliable effective mobility (see Supporting Information **Table S1**).

To investigate the microstructure of the MQW $NFPI_7$ perovskite films, AFM and XRD measurements were made using a Park XE7 scanning probe microscope in non-contact mode and a Philips CuKα X-ray diffractometer, respectively.

Electron Microscopy: To image the cross-sectional structure of the In_2O_3/ZnO/ $NFPI_7$ sample on the Si/SiN_x substrate a thin lamella was prepared by focused ion beam milling in a scanning electron microscope (Helios 400s, FEI). Before milling, the sample was protected by depositing carbon and platinum layers using an electron beam (3 kV, 2.7 nA) and an additional platinum layer using a Ga ion beam (30 kV, 0.28 nA). The bulk of the sample was then milled with the

Ga ion beam (30 kV, 21 nA) to a depth of *ca*. 8-10 μm. The lamella was then extracted from the bulk and attached to a copper TEM grid with the help of a nanomanipulator (omniprobe, AutoProbe300) in accordance with the lift-out method. The lamella was thinned down from both sides reducing the current at each step (30 kV, 2.8 nA to 93 pA). As a final step, the lamella with thickness < 100 nm was treated with a low voltage ion beam (2-5 kV, 10 pA) to remove any damaged areas and surface contaminants. The prepared cross-sectional slice was then analyzed using a TEM (Titan 80-300, FEI) at 300 kV operating voltage. Energy dispersive X-ray spectroscopy spectra were collected in the same microscope in scanning TEM (STEM) mode with Gatan Imaging Filter (GIF) Quantum 966.

Supporting Information

Supporting Information is available online or from the corresponding authors.

Acknowledgements

MUC thanks Durham University and the European Union for a COFUND (No. 609412*)* Durham Junior Research Fellowship. KT and TDA acknowledge financial support from the European Union Horizon 2020 Marie Curie Action: *Flexible Complementary Hybrid Integrated Circuits* (FlexCHIC, N° 658563). DDCB acknowledges the University of Oxford, a Jiangsu Province "Double Creation" Team award, and the Jiangsu Industrial Research Institute for funding. NW, YM, YS and JW acknowledge support from the Major Research Plan of the National Natural Science Foundation of China (N° 91733302), the National Basic Research Program of China (*Fundamental Studies of Perovskite Solar Cells*, N° 2015CB932200), the China - European Union Joint Research Program (N° 2016YFE0112000), the Jiangsu Natural Science Foundation (N° BK20150043 and BK20180085), the National Natural Science Foundation of China (N° 11474164, 61875084 and 61634001), the National

Science Fund for Distinguished Young Scholars (N° 61725502), and the Jiangsu National Synergetic Innovation Center for Organic Electronics and Information Displays.

References

1. G. Xing, N. Mathews, S. S. Lim, N. Yantara, X. Liu, D. Sabba, M. Grätzel, S. Mhaisalkar, T. C. Sum, *Nat. Mater.* **2014**, *13*, 476.
2. F. Deschler, M. Price, S. Pathak, L. E. Klintberg, D. D. Jarausch, R. Higler, S. Hüttner, T. Leijtens, S. D. Stranks, H. J. Snaith, M. Atatüre, R. T. Phillips, R. H. Friend, *J. Phys. Chem. Lett.* **2014**, *5*, 1421.
3. S. D. Stranks, G. E. Eperon, G. Grancini, C. Menelaou, M. J. P. Alcocer, T. Leijtens, L. M. Herz, A. Petrozza, H. J. Snaith, *Science.* **2013**, *342*, 341.
4. J. Burschka, N. Pellet, S. J. Moon, R. Humphry-Baker, P. Gao, M. K. Nazeeruddin, M. Grätzel, *Nature* **2013**, *499*, 316.
5. R. F. Service, *Science.* **2014**, *344*, 6183, 458.
6. Q. Lin, A. Armin, P. L. Burn, P. Meredith, *Nat. Photonics* **2015**, *9*, 687.
7. Q. Lin, A. Armin, R. C. R. Nagiri, P. L. Burn, P. Meredith, *Nat. Photonics* **2015**, *9*, 106.
8. M. A. Green, A. Ho-Baillie, H. J. Snaith, *Nat. Photonics* **2014**, *8*, 506.
9. V. D'Innocenzo, A. R. Srimath Kandada, M. De Bastiani, M. Gandini, A. Petrozza, *J. Am. Chem. Soc.* **2014**, *136*, 17730.
10. V. Gonzalez-Pedro, E. J. Juarez-Perez, W. S. Arsyad, E. M. Barea, F. Fabregat-Santiago, I. Mora-Sero, J. Bisquert, *Nano Lett.* **2014**, *14*, 888.
11. M. Liu, M. B. Johnston, H. J. Snaith, *Nature* **2013**, *501*, 395.
12. H. Zhou, Q. Chen, G. Li, S. Luo, T. B. Song, H. S. Duan, Z. Hong, J. You, Y. Liu, Y. Yang, *Science.* **2014**, *345*, 542.
13. W. S. Yang, J. H. Noh, N. J. Jeon, Y. C. Kim, S. Ryu, J. Seo, S. Il Seok, *Science.* **2015**, *348*, 1234.
14. J. Luo, J. H. Im, M. T. Mayer, M. Schreier, M. K. Nazeeruddin, N. G. Park, S. D. Tilley, H. J. Fan, M. Grätzel, *Science*. **2014**, 345, 1593.
15. Tan, Z.-K. et al. Bright light-emitting diodes based on organometal halide perovskite. *Nat. Nanotech*. **2014**, 9, 687–692.
16. J. Wang, N. Wang, Y. Jin, J. Si, Z. K. Tan, H. Du, L. Cheng, X. Dai, S. Bai, H. He, Z. Ye, M. L. Lai, R. H. Friend, W. Huang, *Adv. Mater.* **2015**, *27*, 2311.
17. H. Cho, S. H. Jeong, M. H. Park, Y. H. Kim, C. Wolf, C. L. Lee, J. H. Heo, A. Sadhanala, N. S. Myoung, S. Yoo, S. H. Im, R. H. Friend, T. W. Lee, *Science.* **2015**, *350*, 1222.
18. N. Wang, L. Cheng, R. Ge, S. Zhang, Y. Miao, W. Zou, C. Yi, Y. Sun, Y. Cao, R. Yang, Y. Wei, Q. Guo, Y. Ke, M. Yu, Y. Jin, Y. Liu, Q. Ding, D. Di, L. Yang, G. Xing, H. Tian, C. Jin, F. Gao, R. H. Friend, J. Wang, W. Huang, *Nat. Photonics* **2016**, *10*, 699.
19. B. R. Sutherland, S. Hoogland, M. M. Adachi, C. T. O. Wong, E. H. Sargent, *ACS Nano* **2014**, *8*, 10947.
20. F. Deschler, M. Price, S. Pathak, L. E. Klintberg, D. D. Jarausch, R. Higler, S. Hüttner, T. Leijtens, S. D. Stranks, H. J. Snaith, M. Atatüre, R. T. Phillips, R. H. Friend, *J. Phys. Chem. Lett.* **2014**, *5*, 1421.

21. I. C. Smith, E. T. Hoke, D. Solis-Ibarra, M. D. McGehee, H. I. Karunadasa, *Angew. Chemie - Int. Ed.* **2014**, *53*, 11232.
22. H. Wei, Y. Fang, P. Mulligan, W. Chuirazzi, H. H. Fang, C. Wang, B. R. Ecker, Y. Gao, M. A. Loi, L. Cao, J. Huang, *Nat. Photonics* **2016**, *10*, 333.
23. S. Yakunin, M. Sytnyk, D. Kriegner, S. Shrestha, M. Richter, G. J. Matt, H. Azimi, C. J. Brabec, J. Stangl, M. V. Kovalenko, W. Heiss, *Nat. Photonics* **2015**, *9*, 444.
24. Y. He, G. Galli, *Chem. Mater.* **2014**, *26*, 5394.
25. C. Wehrenfennig, G. E. Eperon, M. B. Johnston, H. J. Snaith, L. M. Herz, *Adv. Mater.* **2014**, *26*, 1584.
26. C. C. Stoumpos, C. D. Malliakas, M. G. Kanatzidis, *Inorg. Chem.* **2013**, *52*, 9019.
27. X. Y. Chin, D. Cortecchia, J. Yin, A. Bruno, C. Soci, *Nat. Commun.* **2015**, *6*, 7783.
28. F. Maddalena, X. Y. Chin, D. Cortecchia, A. Bruno, C. Soci. *Opt. InfoBase Conf. Pap.*, **2017**. (arXiv: 1710.01900 [physics.app-ph]).
29. F. Maddalena, X. Y. Chin, D. Cortecchia, A. Bruno, C. Soci. *ACS Appl. Mater. Interfaces*. **2018**, 10, 37316-37325.
30. Y. Jia, R. A. Kerner, A. J. Grede, B. P. Rand, N. C. Giebink, *Nat. Photonics* **2017**, *11*, 784.
31. Q. Zhang, R. Su, W. Du, X. Liu, L. Zhao, S. T. Ha, Q. Xiong, *Small Methods,* **2017**, 1,9,1700163.
32. R. Capelli, S. Toffanin, G. Generali, H. Usta, A. Facchetti, M. Muccini, *Nat. Mater.* **2010**, *9*, 496.
33. M. Ullah, Y. H. Lin, K. Muhieddine, S. C. Lo, T. D. Anthopoulos, E. B. Namdas, *Adv. Opt. Mater.* **2016**, *4*, 231.
34. K. Muhieddine, M. Ullah, F. Maasoumi, P. L. Burn, E. B. Namdas, *Adv. Mater.* **2015**, *27*, 6677.
35. J. Zaumseil, R. H. Friend, H. Sirringhaus, *Nat. Mater.* **2006**, *5*, 69.
36. A. J. Heeger, N. S. Sariciftci, E. B. Namdas. "Semiconducting and Metallic Polymers", Oxford University Press, London **2010**.
37. J. Zaumseil, C. L. Donley, J. S. Kim, R. H. Friend, H. Sirringhaus, *Adv. Mater.* **2006**, *18*, 2708.
38. M. U. Chaudhry, K. Muhieddine, R. Wawrzinek, J. Li, S. C. Lo, E. B. Namdas, *ACS Photonics* **2018**, *5*, 2137.
39. N. K. Kumawat, D. Gupta, D. Kabra, *Energy Technol.* **2017**, *5*, 1734.
40. S. P. Senanayak, B. Yang, T. H. Thomas, N. Giesbrecht, W. Huang, E. Gann, B. Nair, K. Goedel, S. Guha, X. Moya, C. R. McNeill, P. Docampo, A. Sadhanala, R. H. Friend, H. Sirringhaus, *Sci. Adv.* **2017**, *3*, e1601935. DOI 10.1126/sciadv.1601935.
41. W. Zou, R. Li, S. Zhang, Y. Liu, N. Wang, Y. Cao, Y. Miao, M. Xu, Q. Guo, D. Di, L. Zhang, C. Yi, F. Gao, R. H. Friend, J. Wang, W. Huang, *Nat. Commun.* **2018**, *9*, 608.
42. M. Yuan, L. N. Quan, R. Comin, G. Walters, R. Sabatini, O. Voznyy, S. Hoogland, Y. Zhao, E. M. Beauregard, P. Kanjanaboos, Z. Lu, D. H. Kim, E. H. Sargent, *Nat. Nanotechnol.* **2016**, *11*, 872.
43. M. Ban, Y. Zou, J. P. H. Rivett, Y. Yang, T. H. Thomas, Y. Tan, T. Song, X. Gao, D. Credington, F. Deschler, H. Sirringhaus, B. Sun, *Nat. Commun.* **2018**, 9, 1.
44. X. Yang, X. Zhang, J. Deng, Z. Chu, Q. Jiang, J. Meng, P. Wang, L. Zhang, Z. Yin, J. You, *Nat. Commun.* **2018**, *9*, *570*. DOI: 10.1038/s41467-018-02978-7.
45. J. Xing et al. Nature Comm. 2**01**8, 9, 3541. DOI: 10.1038/s41467-018-05909-8.
46. J. G. Labram, Y. H. Lin, T. D. Anthopoulos, *Small* **2015**, *11*, 5472.
47. C. H. Ahn, J. M. Triscone, J. Mannhart, *Nature* **2003**, *424*, 1015.
48. H. Faber, S. Das, Y. H. Lin, N. Pliatsikas, K. Zhao, T. Kehagias, G. Dimitrakopulos, A. Amassian, P. A. Patsalas, T. D. Anthopoulos, *Sci. Adv.* **2017**, *3*, 3.

49. J. M. Williamson, R. J. Bowling, R. L. McCreery, *Appl. Spectrosc.* **1989**, *43*, 372.
50. D. H. Cao, C. C. Stoumpos, O. K. Farha, J. T. Hupp, M. G. Kanatzidis, *J. Am. Chem. Soc.* **2015**, *137*, 7843.
51. C. Linghu, S. Zhang, C. Wang and J. Song. *npj Flexible Electronics*. **2018**, 2, 12.
52. L. N. Quan, M. Yuan, R. Comin, O. Voznyy, E. M. Beauregard, S. Hoogland, A. Buin, A. R. Kirmani, K. Zhao, A. Amassian, D. H. Kim, E. H. Sargent, *J. Am. Chem. Soc.* **2016**, *138*, 2649.
53. D. Khim, Y. H. Lin, S. Nam, H. Faber, K. Tetzner, R. Li, Q. Zhang, J. Li, X. Zhang, T. D. Anthopoulos, *Adv. Mater.* **2017**, *29*, DOI 10.1002/adma.201605837.
54. Y. Zhou, C. Fuentes-Hernandez, J. Shim, J. Meyer, A. J. Giordano, H. Li, P. Winget, T. Papadopoulos, H. Cheun, J. Kim, M. Fenoll, A. Dindar, W. Haske, E. Najafabadi, T. M. Khan, H. Sojoudi, S. Barlow, S. Graham, J. L. Brédas, S. R. Marder, A. Kahn, B. Kippelen, *Science.* **2012**, *336*, 327.
55. H. H. Choi, K. Cho, C. D. Frisbie, H. Sirringhaus, V. Podzorov, *Nat. Mater.* **2017**, *17*, 2.
56. J. C. de Mello, H. F. Wittmann, R. H. Friend, *Adv. Mater.* **1997**, *9*, 230.

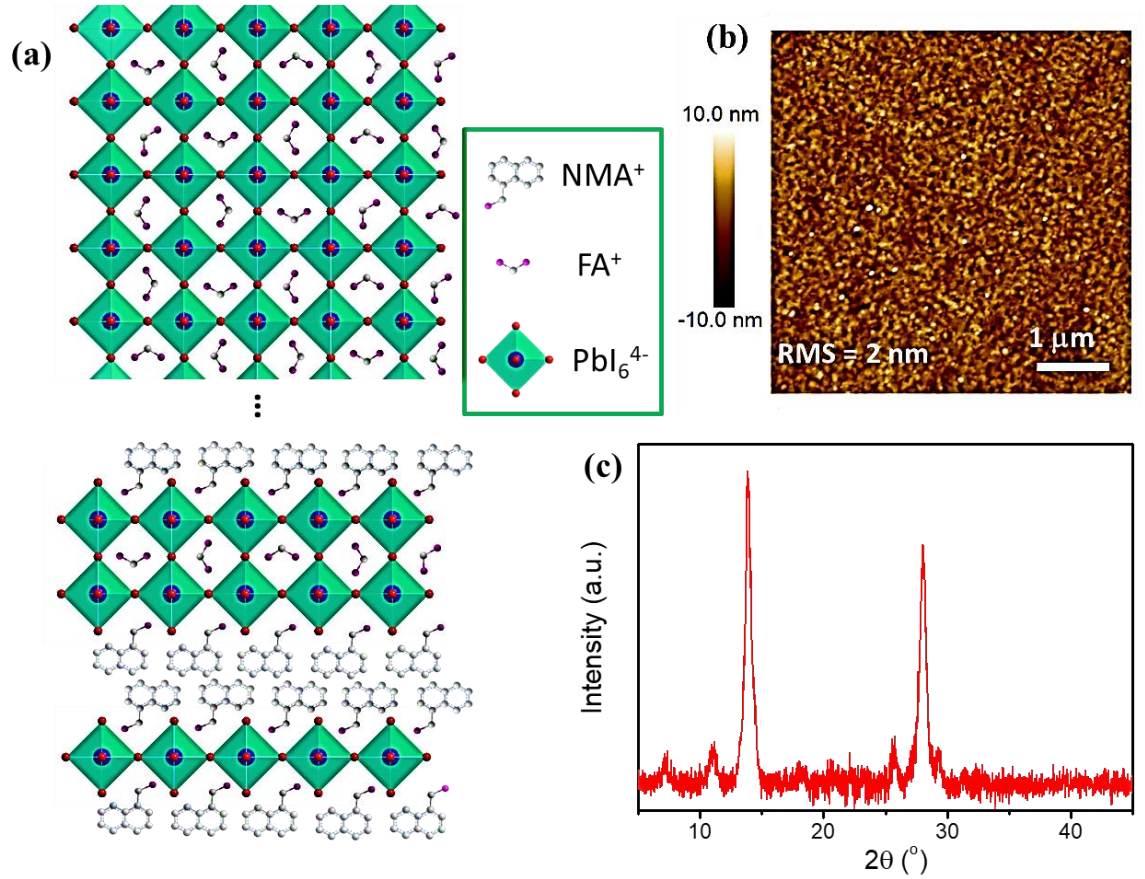

Figure 1. $NFPI_7$ film composition and structure: (a) Schematic MQW perovskite structure comprising NMA^+-separated single layer (bottom), double layer (middle), through to multilayer (top) lead iodide planes. For other than the single layer, compensating FA^+ cations are intercalated within these planes. (b) AFM topographic image and (c) XRD pattern for a 20 nm thickness $NFPI_7$ film deposited on top of an In_2O_3/ZnO/PEIE coated spectrosil substrate. The XRD peaks at 13.9 and 28.1° correspond to (111) and (222) planes for $FAPbI_3$ and the other peaks at 7.3, 11.0, 25.7 and 29.3° are attributed to layered perovskites.

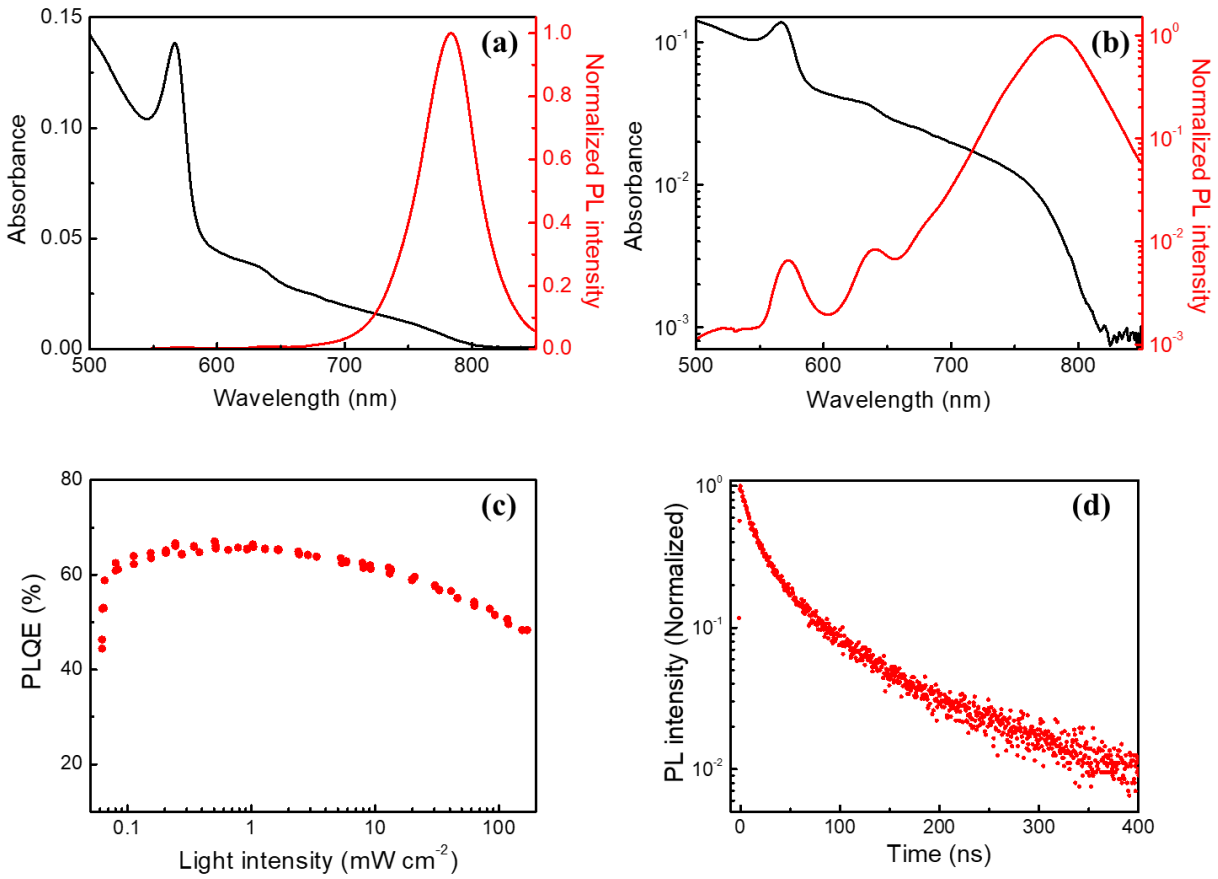

Figure 2. Optical properties for 20 nm thickness $NFPI_7$ films deposited on ZnO/PEIE coated spectrosil substrates. (a) Optical absorbance (black line, left ordinate) and photoluminescence emission (red line, right ordinate) spectra. (b) Data from (a) replotted with a logarithmic ordinate scale to more clearly show the subsidiary peaks. (c) Excitation-intensity-dependent PLQE and (d) time-resolved 783 nm PL decay. In all cases the PL was excited at 445 nm.

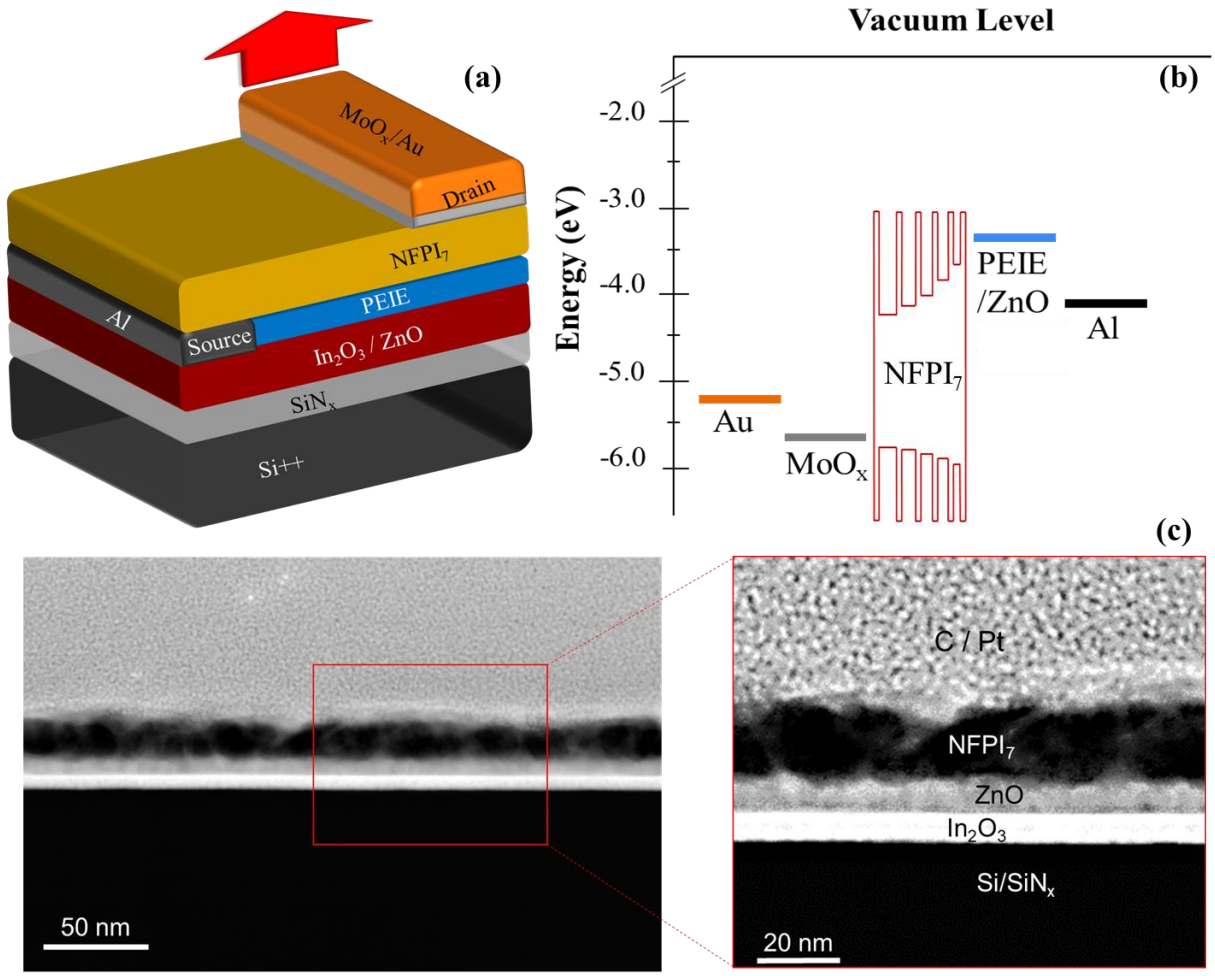

Figure 3. NFPI$_7$-based PeLEFET device structure and energy levels. (a) Schematic device structure. The red arrow indicates the drain contact region from which emission emanates. (b) Energy level diagram. The NFPI$_7$ MQW structure is shown schematically as a series of wells of different width (the barriers are artificially kept fixed for simplicity) (c) STEM cross-sectional image of a device structure minus the top drain electrode. The structures were capped with a carbon/platinum protective layer. Note the exceptional planarity of the solution deposited In_2O_3 layer and the uniformity of its interface with ZnO.

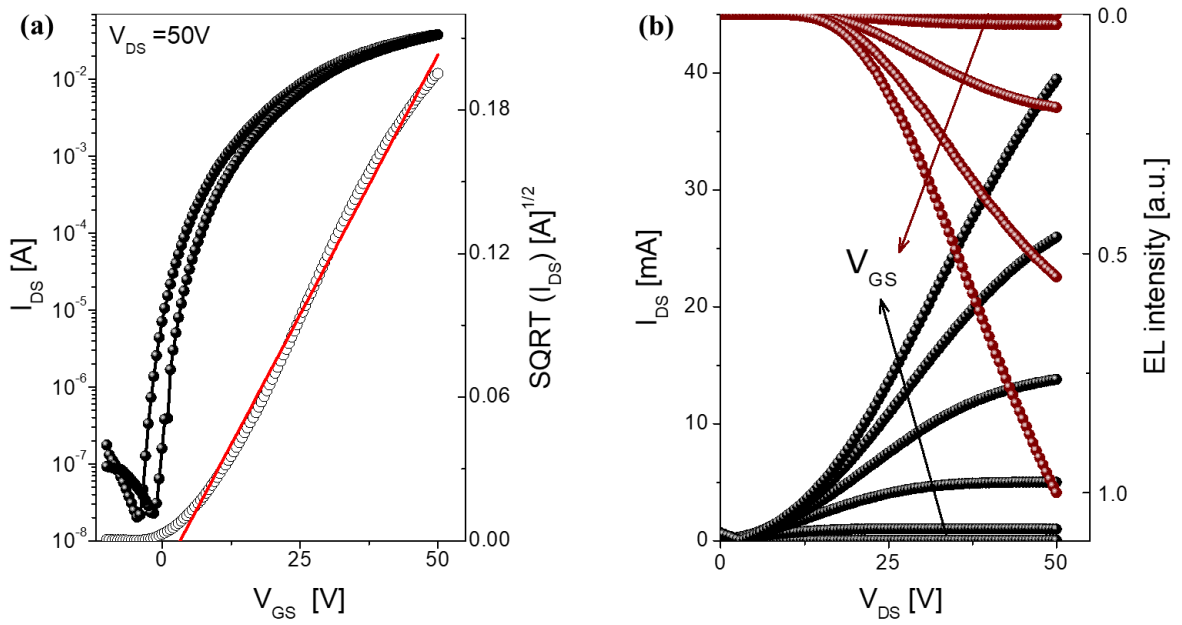

Figure 4. (a) $NFPI_7$-based PeLEFET electrical transfer characteristics (I_{DS} *vs* V_{GS}, filled black circles and line) at V_{DS} =50V. Also shown is a square root plot of the drain current in forward direction versus gate voltage (open circles) together with linear fit (red line). (b) Electrical (I_{DS} vs V_{DS}, filled black circles) and electroluminescence (EL vs V_{DS}, filled red circles) PeLEFET output characteristics. The arrows show the direction of change with increasing V_{GS} (data shown for V_{GS} = 0 V to 50 V with an increment of 10 V).

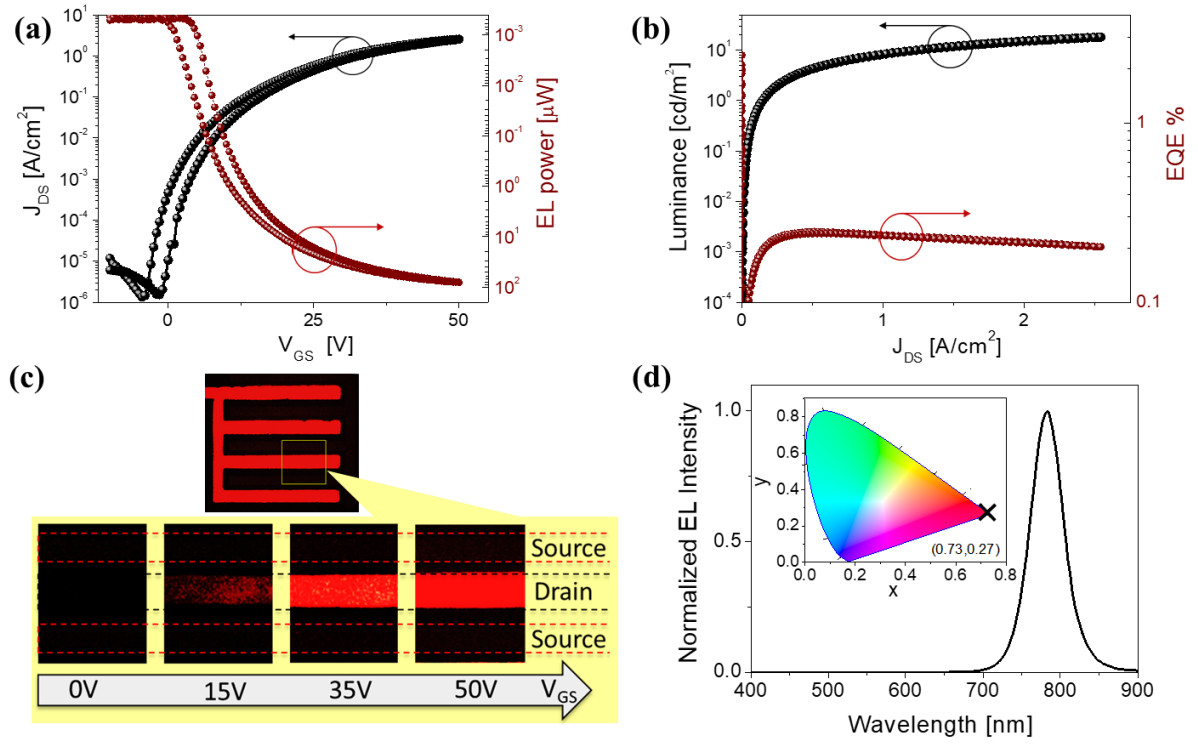

Figure 5. (a) Typical current-density (filled black circles) - gate voltage - EL power (filled red circles, inverted scale) characteristics for a NFPI$_7$-based PeLEFET. (b) Luminance (filled black circles) and EQE % (filled red circles) plotted versus current density. (c) Optical micrographs of the top-emission EL observed during PeLEFET operation. The upper image shows the whole device area at V_{GS} = 50 V and the lower sequence of images, with increasing V_{GS} from left to right (labelled below), show an expanded region containing a length of one of the drain electrode fingers at its centre. (d) EL spectrum of a typical PeLEFET. The spectrum peaks at 783nm with 50 nm full-width at half maximum linewidth. The red colour seen in (c) corresponds to the visible part of this spectrum with highly saturated Commission Internationale d'Eclairage (CIE) color co-ordinates (0.73, 0.27) (see cross in the inset CIE chart).

Table 1. Comparison of PeLEFET performance for this study and literature reports.

PeLEFET parameter	**This study**	**Reference # 27**	**Reference # 28**	**Reference # 29**
Device architecture	Heterostructure: n-type: In_2O_3 / ZnO p-type: $NFPI_7$	Single layer: methylammonium lead iodide ($CH_3NH_3PbI_3$)	Single layer: methylammonium lead iodide ($CH_3NH_3PbI_3$)	Single layer: methylammonium lead iodide ($CH_3NH_3PbI_3$)
Operation mode	Room temperature DC-driven	Low/room temperature DC-driven	Low/room temperature DC-driven / AC-driven	Low temperature DC-driven / AC-Driven
PLQE %	(for $NFPI_7$ film) 66 (at 300K)	(not reported)	(not reported)	(not reported)
Mobility $cm^2 V^{-1} s^{-1}$	$\mu_e \approx 20$ (at 300K)	$\mu_h \approx 7.2x10^{-2}$ (at 78 K) $\mu_e \approx 2.1x10^{-2}$ (at 78 K) & $\mu_h < 1x10^{-5}$ (at 300 K) $\mu_e < 1x10^{-6}$ (at 300 K)	$\mu_h \approx 0.025$ (at 78 K) $\mu_e \approx 0.11$ (at 78 K) & $\mu_h \approx 2x10^{-5}$ (at 300 K) $\mu_e \approx 5x10^{-6}$ (at 300 K)	$\mu_h \approx 0.025$ (at 78 K) $\mu_e \approx 0.11$ (at 78 K)
Current on/off ratio	(for electrons) $\sim 10^6$ (at 300K)	$\sim 10^4$ (at 300K)	~ 50 (at 300K) $\sim 10^3$ (at 78K)	~ 50 (at 300K) $\sim 10^3$ (at 78K)
EQE %	0.2	(not reported)	(not reported)	(not reported)
Luminance cd/m^2	18	(not reported)	(not reported)	0.00460 (at 300K) 0.94 (at 78K)

Supporting Information for:

Light-emitting transistors based on solution processed heterostructures of self-organized multiple quantum well perovskite and metal-oxide semiconductors

Mujeeb Ullah Chaudhry,[*1] *Nana Wang,*[2] *Kornelius Tetzner,*[3] *Akmaral Seitkhan,*[4] *Yanfeng Miao,*[2] *Yan Sun,*[2] *Michael C. Petty,*[1] *Thomas D. Anthopoulos,*[*3, 4] *Jianpu Wang,*[*2] *Donal D.C. Bradley*[*5]

[1] Department of Engineering, Durham University, Lower Mount Joy, South Road, Durham, DH1 3LE, United Kingdom.

[2] Key Laboratory of Flexible Electronics (KLOFE) & Institute of Advanced Materials (IAM), Jiangsu National Synergetic Innovation Center for Advanced Materials (SICAM), Nanjing Tech University (NanjingTech), 30 South Puzhu Road, Nanjing 211816, P.R. China.

[3]Department of Physics and Centre for Plastic Electronics, Blackett Laboratory, Imperial College London, London SW7 2BW, United Kingdom.

[4] King Abdullah University of Science and Technology (KAUST), KAUST Solar Center, Physical Science and Engineering Division, Thuwal 23955, Saudi Arabia.

[5] Departments of Physics and Engineering Science, Division of Mathematical, Physical and Life Sciences, University of Oxford, 9 Parks Road, Oxford OX1 3PD, United Kingdom.

*Address correspondence to: mujeeb.u.chaudhry@durham.ac.uk; iamjpwang@njtech.edu.cn; thomas.anthopoulos@imperial.ac.uk; donal.bradley@mpls.ox.ac.uk

Figure S1: TEM images, superimposition of the separate elements to one EDX map.

Figure S2: Transmittance of the drain (MoO_x/Au) electrode.

Reliability factor and effective mobility calculation.

Figure S3: Linear fit to the transfer characteristics.

Table S1: Calculated mobility, reliability factor and effective mobility.

Calculation of recombination efficiency.

Table S2: Internal Quantum efficiency, PLQY, and singlet-triplet ratios.

Figure S4: EL power and EQE vs. gate voltage.

Figure S5: Working mechanism.

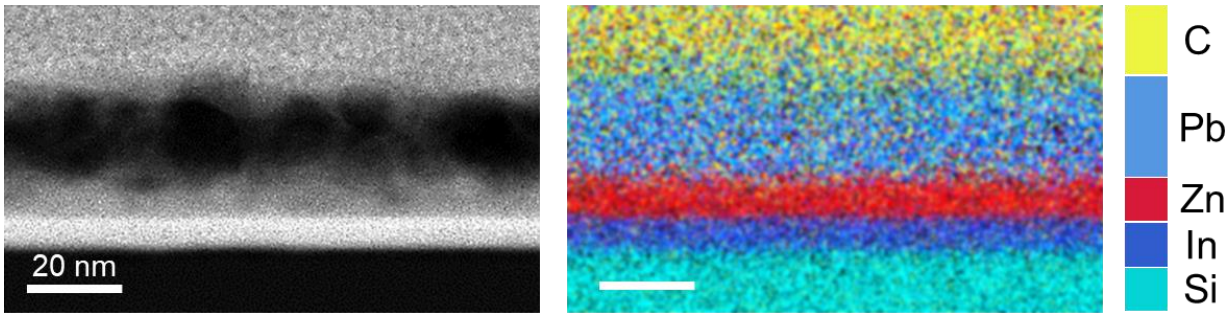

Figure S1: TEM image, superimposition of the separate elements to one EDX map. All elemental maps confirm low intermixing of the materials and distinctive boundaries between the layers. Oxygen map shows its high concentration in the oxides layers as expected, low content of it in the perovskite layer, and high concentration in the top protective layer. The lamella can be further thinned down to see more details like crystal structure of the oxides, however, not the perovskite layer.

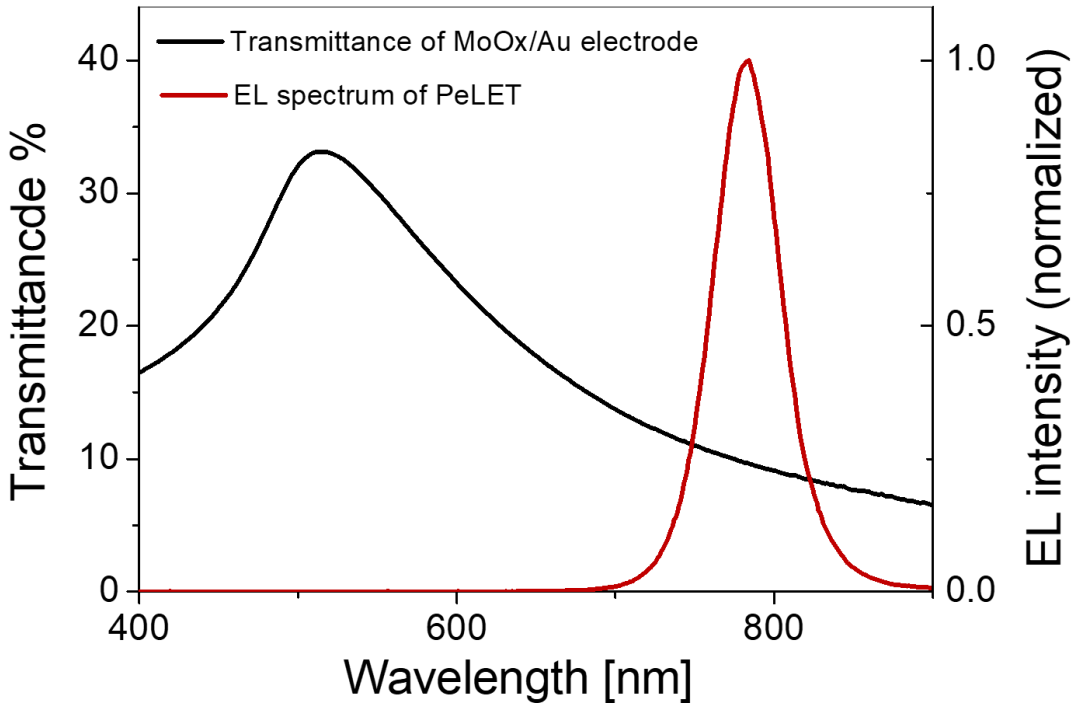

Figure S2: Transmittance of the hole injecting (MoO_x/Au) electrode and electroluminescence under the electrode.

Mobility calculation and reliability factor:

The reliability factor, r, in the FET mobility measurements describes deviation of the behavior of reported FETs from the simple linear increase of conductivity with gate voltage (assuming a constant mobility and negligible threshold voltage). Reliability factor, thus defined as the ratio of the experimentally determined FET channel conductivity at the maximum applied gate voltage to the FET channel conductivity expected in an ideal FET at the same maximum gate voltage (using calculated mobility μ and same device parameters)[44]. In the saturation regime, reliability factor, r_{sat} is calculated as:

$$r_{sat} = \left[\frac{\sqrt{|I_{SD}|^{max}} - \sqrt{|I_{SD}|^{0}}}{|V_{GS}|^{max}}\right]^2 \Big/ \left[\frac{WC_i}{2L}\,\mu_{sat}\right]_{calculate} = \left[\frac{\sqrt{|I_{SD}|^{max}} - \sqrt{|I_{SD}|^{0}}}{|V_{GS}|^{max}}\right]^2 \Big/ \left[\frac{\partial\sqrt{|I_{SD}|}}{V_{GS}}\right]^2_{calculated} \quad (1)$$

Here, μ_{sat} is the experimentally calculated mobility, L, W and C_i are the channel length, channel width can geometric capacitance respectively. $|I_{SD}|^{max}$ is the experimentally determined source-drain current at the $|V_{GS}|^{max}$, and $|I_{SD}|^{0}$ is the source-drain current at $V_{GS} = 0$.

The effective mobility 'μ_{eff}' is the claimed mobility value at the reliability factor of 100% and is calculated as:

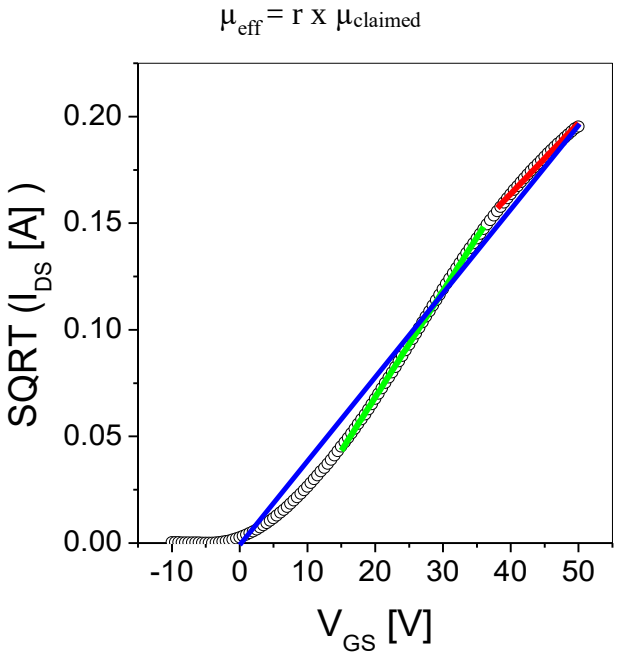

Figure S3: Double slope linear fitting SQRT(I_{DS}) versus V_{GS} data HLEFETs. However, we believe 22 cm^2 V^{-1} s^{-1} is the accurate value, as suggested by recent report.[51]

Table S1: Calculated mobility, reliability factor and effective mobility.

Linear Fit range	$\mu_{calculated}$ (cm^2 V^{-1} s^{-1})	r %	μ_{eff} (cm^2 V^{-1} s^{-1})
Red	14	144%	20.2
Blue	20.2	100%	20.2
Green	28.5	71%	20.2

Internal Quantum efficiency (IQE):

The external quantum efficiency (EQE) is the ratio of photons emitted from the device to the number of electrons injected. The measured EQE is given by the below given equation:

$$\emptyset_{EQE} = \emptyset_{out} \times \emptyset_R \times \emptyset_{S-T} \times \emptyset_{PLQE}$$

where ϕ_{out} is the out-coupling efficiency (light extraction from the device), $\phi_{S\text{-}T}$ is a spin statistics factor relating to the singlet and triplet ratio, and ϕ_{PLQY} is the photoluminescence quantum yield. ϕ_R is radiative recombination efficiency is a measure of the percentage of electrons and holes that form excitons in the material, i.e. the recombination efficiency or IQE. Using the PLQE and the EQE at highest current density PeLEFETs, the recombination efficiency can be calculated from above equation. The spin factor is given as 25% for fluorescent materials. The IQE of PELEFTE is shown in Table S2.

Table S2: Recombination efficiency, PLQY, and singlet-triplet ratios

Device	ϕ_{EQE}	ϕ_{out}	$\phi_{S\text{-}T}$	ϕ_{PLQY}	ϕ_R
PeLEFET	0.2%	20%	25%	66%	6%

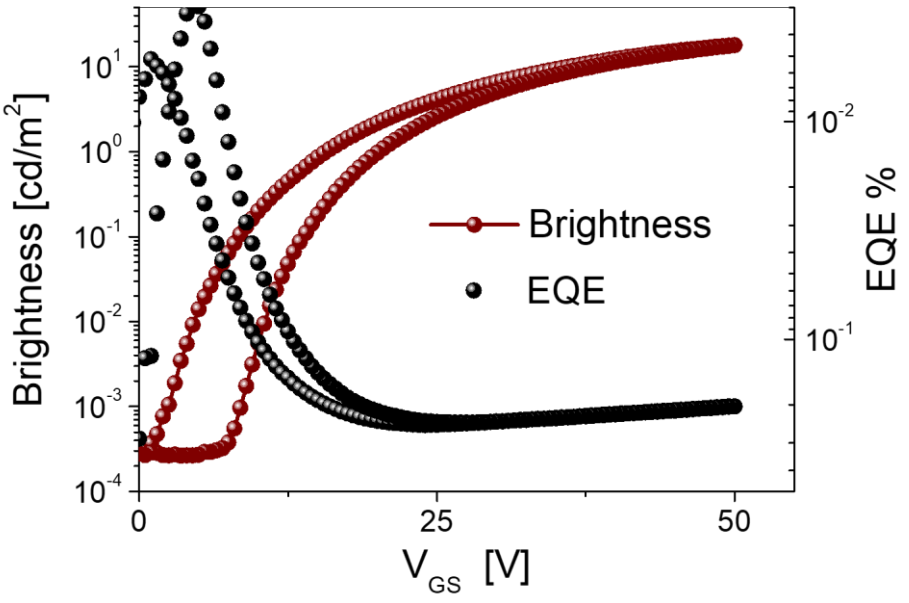

Figure S4: Brightness and EQE of PeLEFETs as a function of gate bias.

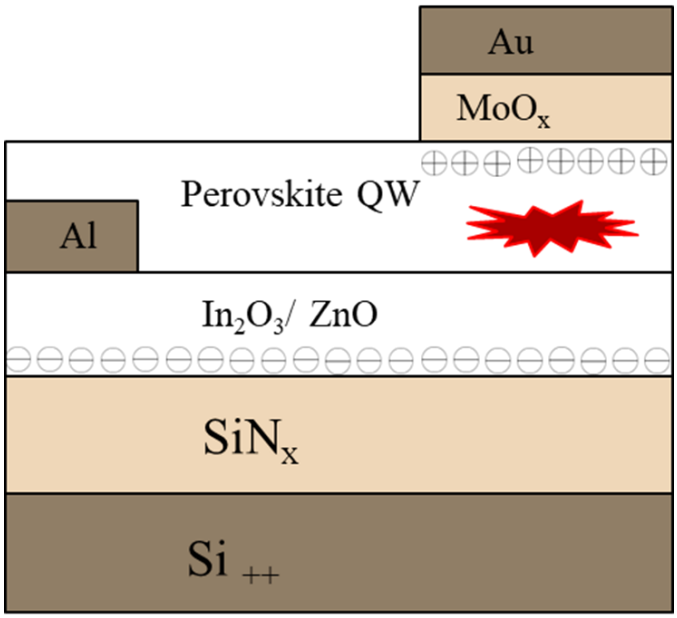

Figure S5: Working mechanism of PeLEFETs.